Extreme Mechanics Letters 37 (2020) 100724

Contents lists available at ScienceDirect

Extreme Mechanics Letters

journal homepage: www.elsevier.com/locate/eml

Prestress-controlled asymmetric wave propagation and reciprocity-breaking in tensegrity metastructure

Yitian Wang [a], Weijia Zhao [a], Julian J. Rimoli [b], Rui Zhu [a,*], Gengkai Hu [a,*]

[a] School of Aerospace Engineering, Beijing Institute of Technology, Beijing, China
[b] School of Aerospace Engineering, Georgia Institute of Technology, Atlanta, GA, United States

ARTICLE INFO

Article history:
Received 15 January 2020
Received in revised form 3 April 2020
Accepted 3 April 2020
Available online 9 April 2020

Keywords:
Prestress control
Tensegrity metastructure
Asymmetric wave propagation
Non-reciprocal

ABSTRACT

In this letter, prestress is harnessed to break the spatial or/and time wave reciprocity and realize asymmetric elastic wave propagations in the full elastodynamic context. Unlike other asymmetric wave systems that rely on the complicated microstructures or multi-physical coupling, the proposed metastructure is simply constructed with repetitive prismatic tensegrity cells (PTCs) where prestress exists intrinsically. By investigating the prestress-trigged wave mode selection and conversion phenomena with a theoretical model, we developed a new approach to achieve asymmetric elastic wave propagation in the metastructure with modulated prestress distribution in space. Furthermore, by expanding the prestress tuning in both space and time domains, the elastodynamic reciprocity is finally broken in the tensegrity metastructure without introducing nonlinearity or external bias fields to the system. Due to the simple construction and intrinsic tunability, the proposed tensegrity metastructure design can be potentially useful in various applications, such as vibration isolation and elastic wave communication.

1. Introduction

Elastodynamic reciprocity is a fundamental principle that applies to both standing and propagating waves in linear structures [1]. Due to elastodynamic reciprocity, band structures of time-invariant linear elastic material are symmetric about its origin point $k = 0$, implying that waves propagate symmetrically in opposing directions [2,3]. Breaking elastodynamic reciprocity can lead to asymmetric elastic wave propagation [4–9], which has great potential for applications in various engineering fields, such as vibration mitigation, elastic wave communication and structural health monitoring.

In recent years, increased interest in designing elastic metamaterials or metastructures with artificial microstructures to achieve asymmetric wave propagations has been witnessed [10–15]. For example, Zhu [10] proposed a metamaterial plate with time-invariant linear microstructures, which function as a wave mode converter as well as a selective wave mode mirror, to achieve asymmetric elastic wave propagation while still obeying elastodynamic reciprocity. To truly break elastodynamic reciprocity without external bias field, nonlinear [11,12] or spatiotemporally varying properties [14–16] should be introduced into the passive material system. Boechler [11] and Wallen [12] harnessed contact and geometric nonlinearity, respectively, to achieve non-reciprocal elastic wave propagation in elastic materials. Vila [13] systematically investigated the non-reciprocal dispersion properties of 1D linear elastic discrete system with periodic time-varying coefficients. Nassar [14–16] theoretically studied elastic metamaterials with modulated material properties in both spatial and time domains, which results in asymmetric elastic wave propagations. However, such analytical models are far away from physical realization. To realize metamaterials with reciprocity-breaking ability, additional active elements and controlling circuits are added to the elastic microstructures [17–19]. Still, those metamaterial/metastructure designs strongly rely on the expensive microstructures and additional control systems. Also, the lack of easy tunability hinders the implementation of real applications of asymmetric wave propagation systems.

The introduction of electromechanical or magnetomechanical coupling materials into the metastructure building blocks provides a promising method to actively tune the overall wave behavior. However, this can lead to large costs associated to the presence of complicated external circuits and fabrication complexity [20–25]. On the other hand, prestress has been leveraged to achieve various elastic wave manipulations in the full elastodynamic context, such as broadband elastodynamic cloaking [26,27] and stop bands control [28] in nonlinear elastic materials. Most recently, the studies on prestress-controlled wave propagation in tensegrity metastructures open a new avenue for

* Corresponding authors.
E-mail addresses: ruizhu@bit.edu.cn (R. Zhu), hugeng@bit.edu.cn (G. Hu).

https://doi.org/10.1016/j.eml.2020.100724

achieving simultaneous elastic wave controllability and easy tunability in a linear structure where geometrical nonlinearity and prestress-controlled elasticity can be found intrinsically [29–31].

In this letter, two kinds of tensegrity metastructures with spatially-modulated time-invariant and spatiotemporally varying prestress are designed to realize asymmetric and non-reciprocal elastic wave propagation, respectively. The letter is arranged in the following order. First, a theoretical model with coupled axial-torsional effective stiffness is developed to study the wave mode selection and conversion phenomena in the proposed metastructure consisting of prismatic tensegrity cells (PTCs). Then, tunable asymmetric elastic wave propagation is demonstrated by harnessing the aforementioned wave phenomena with spatially modulated prestress in the unaltered tensegrity metastructure. Finally, non-reciprocal elastic wave propagation is realized by expanding the prestress control in a tensegrity metastructure with time–space modulation.

2. Theoretical model for prestress-controlled elastic wave propagation in tensegrity metastructures

Fig. 1a shows the schematic of the PTC configuration. The PTC consists two Aluminum (Al) disks at the top and bottom ends with three Nylon cross-strings (gray colored) and three polylactic acid (PLA) bars (yellow colored) between the disks. The properties of each components of the PTC are listed in Table 1. It should be noticed that without prestress in its building components, the PTC is an under-constrained system and cannot keep its own shape [32,33]. Therefore, prestress is an intrinsic property of a PTC and the following metastructures.

In Fig. 1a, the prestress in a PTC's string components, P_s, can be determined as:

$$P_s = k_s(L_{s0} - L_{sn}) \tag{1}$$

where k_s is the string's stiffness, L_{sn} and L_{s0} are the nature length of the strings and the length when the PTC is in its unloaded equilibrium position. Since a stable unloaded structure requires the relative angle of the PTC's two end-disks to be $\frac{5\pi}{6}$ [29], the relation between L_{s0} and the PTC's geometrical parameters can be obtained:

$$L_{s0} = \sqrt{(2-\sqrt{3})R^2 + h^2} \tag{2}$$

And the prestress of the bars, P_b, has the following relationship with P_s

$$P_b = -\frac{\sqrt{(2+\sqrt{3})R^2 + h^2}}{\sqrt{(2-\sqrt{3})R^2 + h^2}} P_s \tag{3}$$

The right-handed chiral arrangement of the PTC's bars and strings also offers a unique compression–rotation coupling, as shown in Fig. 1a. To describe this coupling effect, an equivalent model has been developed with an effective stiffness matrix [30] and the constitutive equation is

$$\begin{Bmatrix} F \\ T \end{Bmatrix} = \begin{bmatrix} k_h & k_c \\ k_c & k_m \end{bmatrix} \begin{Bmatrix} u \\ \theta \end{Bmatrix} \tag{4}$$

where the two diagonal components of the 2 * 2 matrix are the compression stiffness k_h and the rotation stiffness k_m, respectively. The off-diagonal components, k_c, describe the aforementioned compression–rotation coupling. By taking the partial derivatives of the torque, T, and axial force, F, which are both functions of u and θ, the prestress-related stiffness components can be obtained.

A finite element (FE) model is also introduced to validate the equivalent model with the help of commercial FE software ANSYS V18, as shown in Fig. 1b. By understanding the working mechanism of the proposed PTC, shell element, SHELL 281, and spring element, LINK180, are selected for the disks and bars/strings, respectively, to reduce the computational time while maintaining the accuracy of the model. Spherical joints are used at the connections between the strings/bars and the disks to permit the rotational degrees of freedom (DoFs) of the LINK elements. Rigid disk assumption is achieved by applying large elastic modulus to the top and bottom disks. Prestress in the bars and strings are applied with proper configurations in the corresponding LINK180 elements, respectively. Only axial force and torque are applied on the PTC and therefore, only two DoFs, the relative rotational angle, θ, and the relative axial displacement, u, between the two end-disks, are considered.

Prestress plays a key role in the PTC's compression–rotation coupled stiffness. Fig. 1c demonstrates that the stiffness can be tuned by changing the prestress in the strings. Both results obtained from the theoretical and FE models are plotted for comparison purpose. First, very good agreement can be found between the two results suggesting that the equivalent model is accurate enough to capture the coupling effect. Then, a prestress-controlled range for each stiffness matrix component suggests the potential for *in situ* elastic wave propagation tuning in any PTC-based system. Furthermore, the monotonically varying coupling-stiffness with the prestress indicates that an adjustable elastic wave mode conversion can be achieved, which is the key for our prestress-controlled asymmetric elastic wave metastructure which will be explained in detail in the following section.

The prestress-controlled tunable asymmetric wave propagation can be obtained based on the wave mode selection and conversion phenomena in a PTC-based compression–rotation coupled metastructure, as shown in Fig. 2a. For linear elastic wave propagations in the 1D infinite chain consisting of repetitive PTCs, the governing equation of the *nth* cell can be written as

$$\begin{aligned} &-\omega^2 \begin{bmatrix} m & 0 \\ 0 & J \end{bmatrix} \begin{Bmatrix} \tilde{u} \\ \tilde{\theta} \end{Bmatrix} \\ &= \begin{bmatrix} k_h(e^{iqh} + e^{-iqh} - 2) & k_c(e^{iqh} + e^{-iqh} - 2) \\ k_c(e^{iqh} + e^{-iqh} - 2) & k_m(e^{iqh} + e^{-iqh} - 2) \end{bmatrix} \begin{Bmatrix} \tilde{u} \\ \tilde{\theta} \end{Bmatrix} \end{aligned} \tag{5}$$

where $\tilde{u}$ and $\tilde{\theta}$ are the amplitudes of the axial displacement and rotational angle in the first PTC, respectively. An eigenvalue problem can then be formed from Eq. (5) and the dispersion results for two wave modes can be calculated:

$$\begin{aligned} &\omega_{L,H} \\ &= \sqrt{\frac{1-\cos(kh)}{mJ}\left(mk_m + Jk_h \mp \sqrt{(mk_m + Jk_h)^2 - 4mJ(k_m k_h - k_c^2)}\right)} \end{aligned} \tag{6}$$

Both wave modes have compression–rotation coupled motions. The one with lower wave velocity is named as the lower mode wave (L-wave) while the other one with higher wave velocity is the higher mode wave (H-wave). A compression–rotation ratio $Ra^* = \frac{\tilde{u}}{\tilde{\theta}R}$ is defined to better distinguish the two wave modes. By combining Eqs. (5) and (6), the ratios can then be calculated as

$$\begin{aligned} (Ra^*)_{L,H} &= \left(\frac{\tilde{u}}{\tilde{\theta}R}\right)_{L,H} \\ &= \frac{2Jk_c}{R[mk_m - Jk_h \mp \sqrt{(mk_m + Jk_h)^2 - 4mJ(k_m k_h - k_c^2)}]} \end{aligned} \tag{7}$$

Fig. 2b shows that the compression–rotation ratios change with different prestress in the PTC's strings. First, it is interesting to find that the compression and rotational components

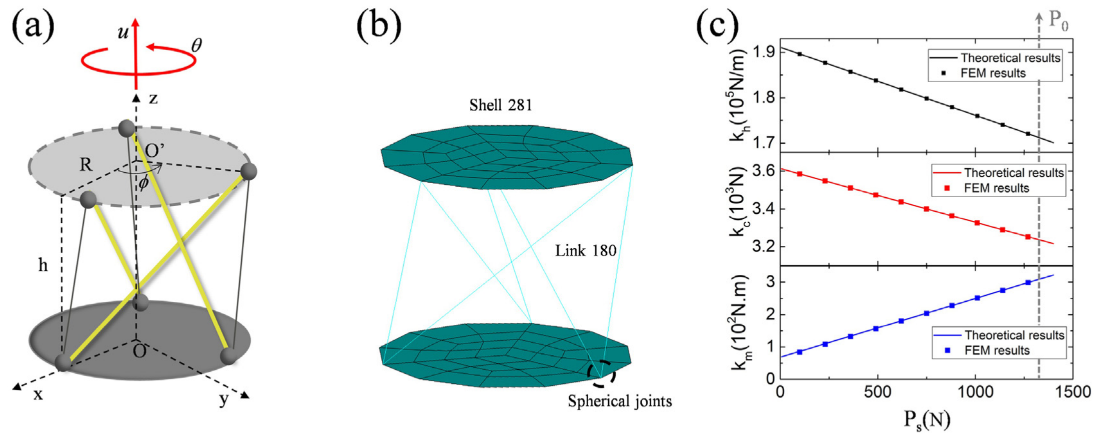

Fig. 1. Reference configuration schematic, FEM model and tunable static stiffnesses of the PTC. (a) Reference configuration schematic of the PTC. (b) FEM model of the PTC. (c) k_h, k_c and k_m change with the prestress of the string. P_0 is the reference prestress.. (For interpretation of the references to color in this figure legend, the reader is referred to the web version of this article.)

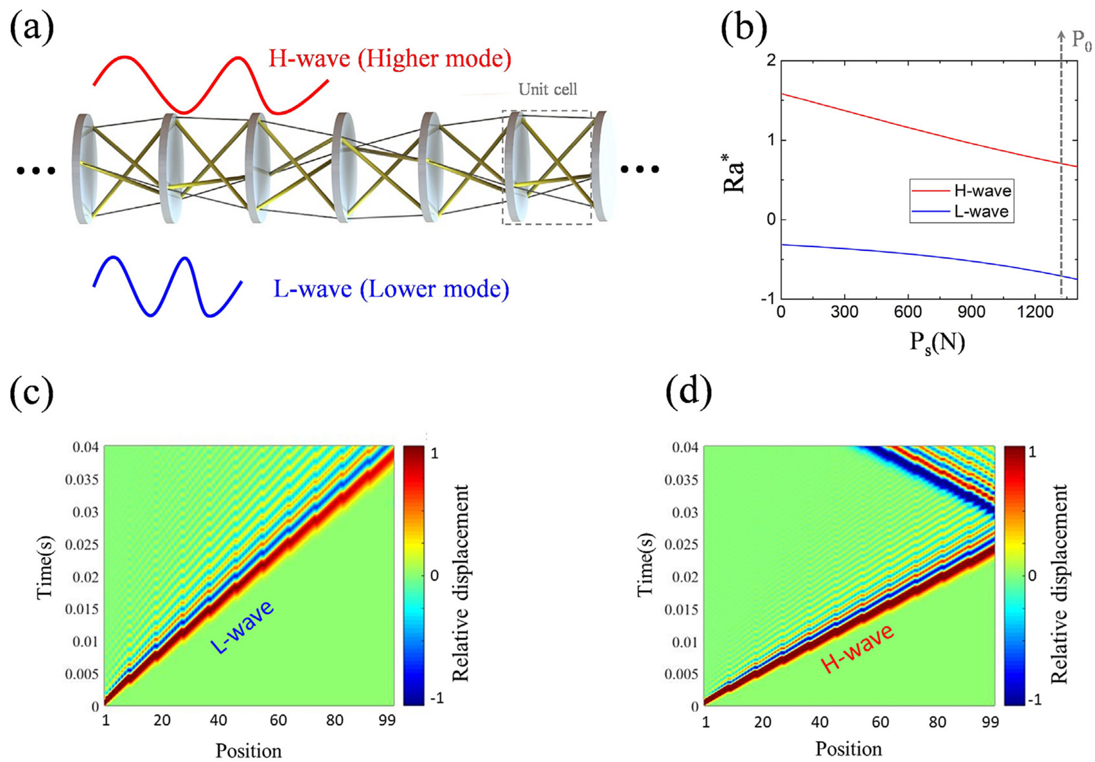

Fig. 2. Schematic and wave property of the 1D PTCs chain. (a) Schematic of repetitive PTCs chain wave system. (b) The Ra^* change with prestress in the strings. (c)(d) FEM relative displacement map, results which represent relative displacement as color intensity with respect to position (horizontal axis) and time (vertical axis) on the pulse excitation input. (c) pulse input, Ra^* equal to −0.7(Ra^* of L-wave). (d) Pulse input, Ra^* equal to 0.7(Ra^* of H-wave).

Table 1
The material and geometrical parameters of the PTC.

Material parameters		Geometrical parameters	
The mass of the disk (m)	$17.3*10^{-3}$ (kg)	Radius of the end-disks (R)	$6.0*10^{-2}$ (m)
Moment of inertia of the disk (J)	$311.0*10^{-7}$ (kg.m^2)	Height of the PTC (h)	$9.5*10^{-2}$ (m)
Stiffness of the bars (k_b)	$5.4*10^4$ (N/m)		
Stiffness of the strings (k_s)	$4.6*10^4$ (N/m)		

of the two waves have inverse and same phases, respectively. Also, it is noted that when the prestress increases, the compression component of the L-wave increases while that of the H-wave decreases, which offers a good way to achieve targeted wave mode conversion via prestress adjustment. Finally, transient wave propagation studies are performed numerically to validate the existence and orthogonality of the two wave modes. In the numerical studies, a metastructure chain made of 100 PTCs is investigated. Convergence tests of both the finite element mesh size and the time steps have been conducted to ensure the accuracy of the numerical results. The right end of the chain is fixed while a pulse displacement excitation is applied to the left end as an

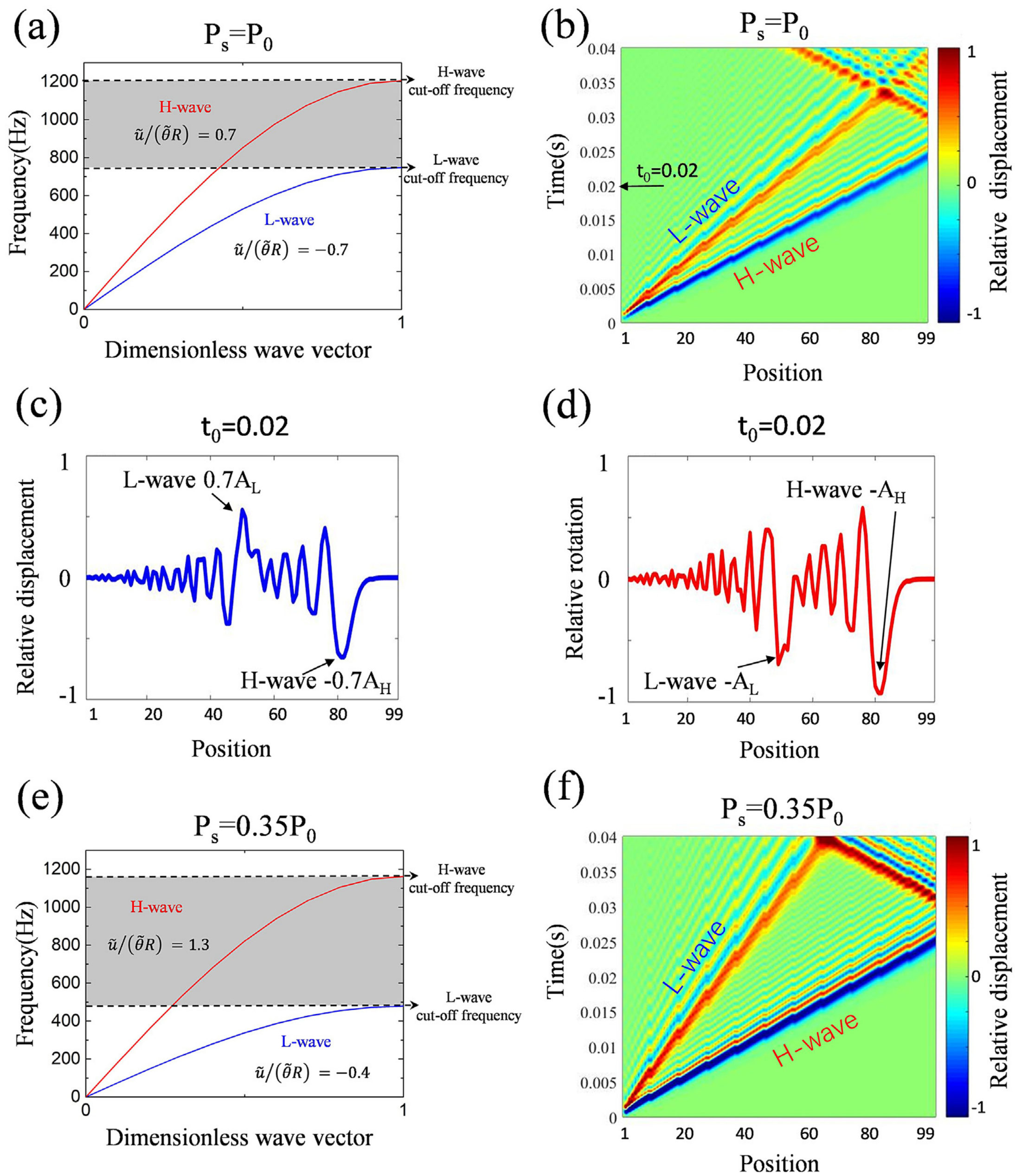

Fig. 3. Dispersion curve and 100 unit cells FEM results with different prestress level. (a)(b)(c)(d) The dispersion curve and FEM result of the chain with prestress P_0. (a) The dispersion curve of the infinite PTC chain system. (b) FEM result with rotation displacement pulse as the input, which represent relative displacement as color intensity with respect to position (horizontal axis) and time (vertical axis). (c) FEM result, the displacement at $t_0 = 0.02$. (d) FEM result, the rotation displacement at $t_0 = 0.02$. (e)(f) The dispersion curve and FEM result of the chain with changed prestress($0.35P_0$). (e) The dispersion curve of the infinite PTC chain system. (f) FEM result of PTC chain with rotation displacement pulse as the input.. (For interpretation of the references to color in this figure legend, the reader is referred to the web version of this article.)

input source with Ra^* being −0.7(L-mode) and 0.7 (H-mode), as shown in Fig. 2(c) and 2(d), respectively. It is noticed that the two wave modes propagate separately without energy exchange to each other, which confirms their independent existences and orthogonality.

The prestress-tuned wave behaviors are analyzed in the proposed PTC-based metastructure. First, the dispersion properties of the two wave modes in the metastructure can be obtained by calculating Eq. (6) and the results are shown in Fig. 3(a). It is found that the L-wave and H-wave have different cut-off frequencies and therefore, only H-wave can pass in the frequency region highlighted as the gray zone. This particular frequency region can further be used for the wave mode selection purpose. Then, the wave mode conversion is investigated. Fig. 3(b)–(d) show the wave propagation results for a purely rotational displacement pulse excitation. Although no axial-displacement exists in the input wave, two waves with axial displacement components can still be found propagating in the chain, as shown in Fig. 3(b). The colored axial displacement map in the figure indicates that the two waves have different wave fronts with negative and positive displacements, respectively. Both axial and rotational displacements in the chain are plotted at time point $t_0 = 0.02$, as shown in Fig. 3(c) and (d), respectively. By calculating the compression–rotation ratio, Ra^*, from the two displacement results, it can be found that Ra^* for the two wave modes are 0.7 and −0.7, which coincide with the previously defined H-wave and L-wave,

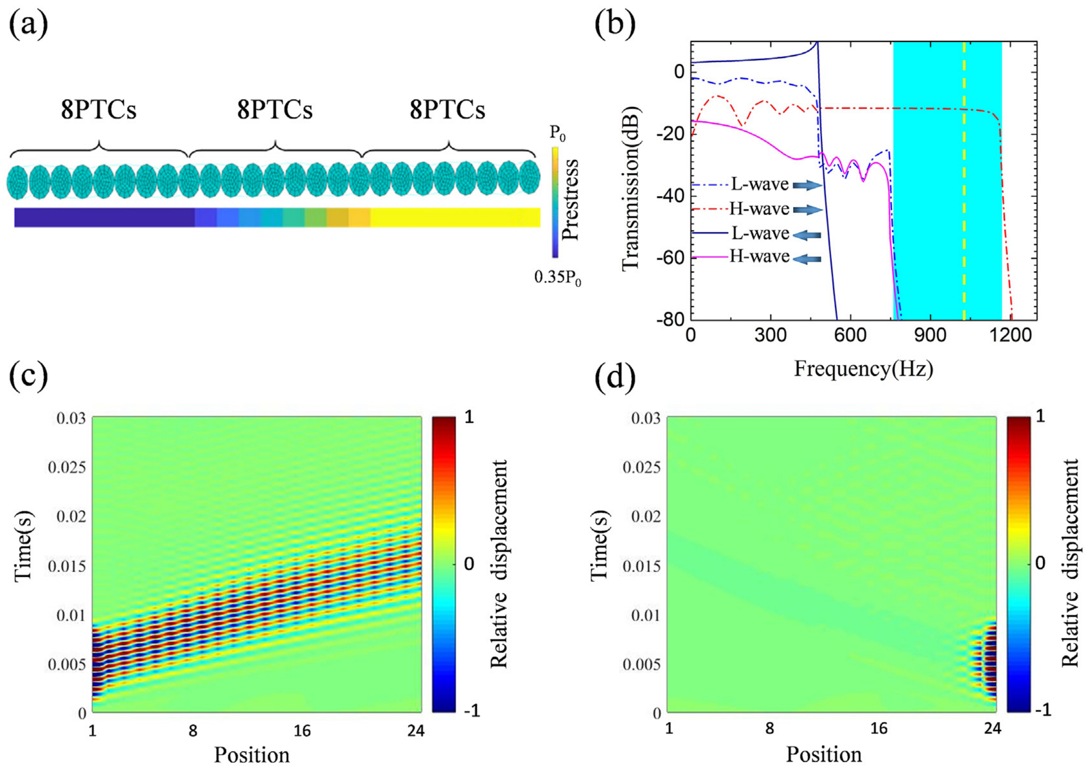

Fig. 4. Asymmetric wave propagation metastructure model designed by the prestress and transfer matrix method result and FE results which represent relative displacement as color intensity with respect to position (horizontal axis) and time (vertical axis). (a) Asymmetric wave propagation metastructure model designed by the prestress. (b) TMM result, L wave ($Ra* = -0.7$) harmonic input with different excitation frequencies. (c)FE result, 10-peak tone burst L wave input with 1000 Hz central frequency, in the left side.(d) FE result, 10-peak tone burst L wave input with 1000 Hz central frequency, in the right side.. (For interpretation of the references to color in this figure legend, the reader is referred to the web version of this article.)

respectively. Therefore, it is confirmed that the purely rotational input wave converses into the two H- and L-type output waves. Finally, the prestress tuning on the wave mode selection and conversion is investigated. Prestress, $P_s = 0.35\ P_0$, is applied to each PTC of the metastructure chain and the altered dispersion curves are shown in Fig. 3(e). It is noticed that changing the prestress cannot only alter the compression–rotation ratios ($(Ra^*)_L$= -0.4 and $(Ra^*)_H = 1.3$) and wave velocities of the two wave modes, but also change their cut-off frequencies, which results in a broader frequency range for the wave mode selection (larger gray zone in the figure). Finally, Fig. 3(d) shows the FE results of wave mode conversion under purely rotational wave input. A decreased L-wave velocity can be found obviously comparing to the results in Fig. 3(c), which confirms the changes in wave mode conversion due to the prestress tuning.

3. Employing prestresses to generate asymmetric wave propagation and break reciprocity

In this section, asymmetric elastic wave propagation is demonstrated by harnessing the aforementioned wave mode selection and conversion phenomena in the tensegrity metastructures with specially designed prestress distribution. Fig. 4(a) shows the schematic of the prestress distribution in the proposed metastructure which, from left to right, consists of 8 PTCs with $P_s = 0.35P_0$, 8 PTCs with gradually increasing P_s whose value between $0.35P_0$ to P_0, and 8 PTCs with $P_s = P0$.

It has been demonstrated in the previous section that the change in prestress can alter the properties of the waves, such as Ra^*, as well as the cutoff frequency of certain wave mode, which provides the basis for the prestress-trigged wave mode conversion and selection, respectively. Fig. 4(b) shows the transmission results of L-type input waves with different excitation frequencies. Two cases, left-to-right and right-to-left propagations, are studied, which are marked with dash-dot and solid lines, respectively. Transfer matrix method (TMM) is used to obtain the results and the details can be found in Appendix A. In the figure, it can be found that the input L-wave can pass from one end to the other in both cases when the excitation frequency is below the wave's cut-off frequency (the lower boundary of the blue shaded zone). Wave mode conversions are clearly observed in both cases since not one but two transmission curves can be found for each incidence. In particular, the notable H-wave transmission curve (pink-color curve) in the right-to-left transmission results is produced by the wave mode conversion (from the excited L-wave $Ra^* = -0.7$) inside the chain. What really interests us happens inside the blue shaded zone, where asymmetric wave propagation is realized since the input wave can only propagate from left to right but not the other way around. To understand how the asymmetric wave propagation is trigged by the prestress distribution in the tensegrity metastructure, detailed investigations are conducted on the wave mode conversion and selection in the blue shaded zone. When the input L-wave ($Ra^* = -0.7$) with excitation frequency at 1000 Hz (inside the blue shaded zone) is applied to the left end, first wave mode conversion happens, which converts the input L-wave into a left end PTC (with $P_s = 0.35P_0$) supported H-wave ($Ra^* = 1.3$). Then, the wave propagates through the middle part PTCs with gradually increasing P_s, where second wave mode conversion happens, which changes the H-wave's Ra^* into 0.7. It is noted that few reflection happens due to the gradient prestress distribution. In the other case, the same L-wave ($Ra^* = -0.7$) is applied to the right end. Instead of wave mode conversion, a wave mode

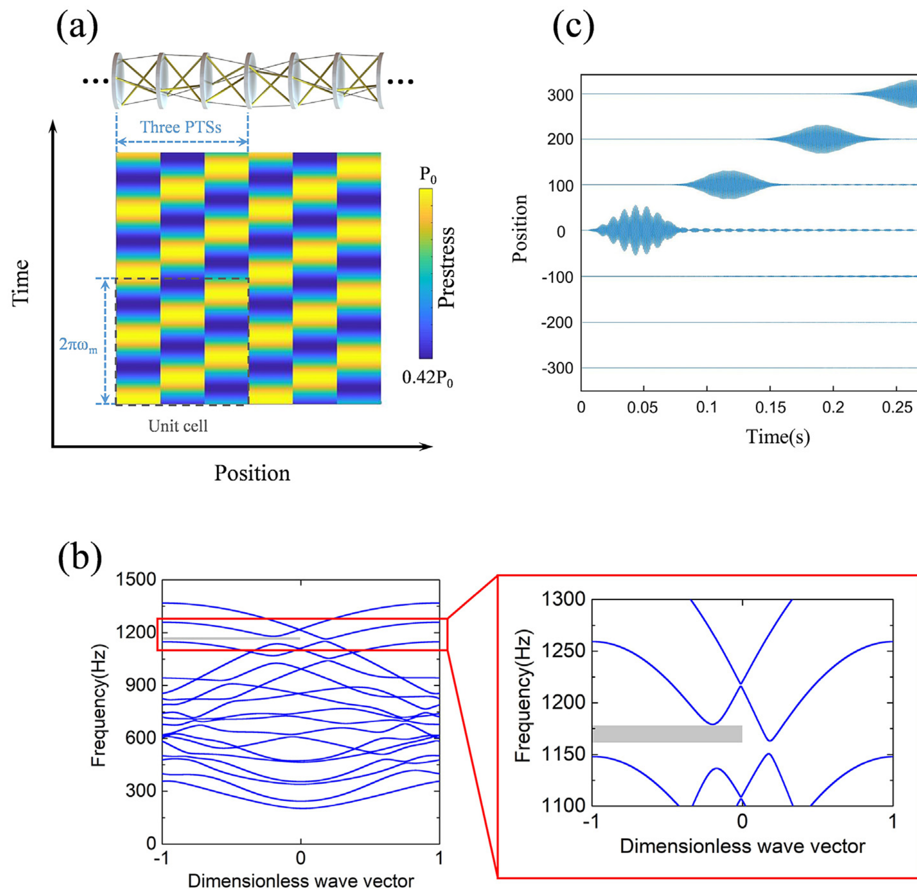

Fig. 5. The time–space modulated prestress, the dispersion result of this system and the numerical result of the 1800 PTCs system with modulated prestress. (a) The time–space modulated prestress. (b) The dispersion result of this system. (c) The numerical result 1800 PTCs with the fix boundary in both end. The input is a 100-peak tone burst force excitation in the center of the system.

selection first happens. Since the blue zone represents the stop band for L-wave but pass band for H-wave ($Ra^* = 0.7$), no input L-wave can pass the right part of the metastructure, which results in a total block of the right-to-left wave propagation. Here, the asymmetric wave propagation is realized by applying specific prestress distributions in all identical PTCs. Since the prestress can easily be altered in tensegrity's strings without any changes in its elastic components, *in-situ* tuning of asymmetric wave propagation's direction as well as frequency range can be achieved.

In order to validate the prestress design with a transient asymmetric wave propagation, FE simulations are performed by inputting a 10-peak tone burst L-wave excitation with 1000 Hz central frequency, $A_0(1 - \cos(2\pi f_c t/10)) \times \sin(2\pi f_c t)$, to each end of the tensegrity metastructure. The results of left-to-right and right-to-left wave transmissions are shown in Fig. 4c and 4d, respectively. Since the input wave is within the blue shaded zone, wave mode conversion happens in Fig. 4c which results in part of the wave energy being transmitted to the right end, while wave mode selection totally blocks the L-wave energy reaching the left end, as shown in Fig. 4d.

The designed prestress distribution in spatial domain can lead to asymmetric wave propagation with, however, unchanged reciprocity in the metastructure. Here, we extend the prestress distribution design in both spatial and time domains in order to realize non-reciprocal elastic wave propagation in the tensegrity metastructure. The prestress tuning could be achieved in practice, for example, with a hydraulic actuator. To break the time-reversal symmetry, we introduce time–space modulated prestress in the PTCs of the metastructure, as shown in Fig. 5a. A traveling wave-like space–time domain modulation is applied and the prestress of the nth PTC is $P_0 + 0.58P_0 \times \sin(\frac{2\pi \cdot nh}{WL_m} - \omega_m t)$, where $\omega_m = 628$ rad/s is chosen as the angular frequency of the time-domain modulation while $WL_m = 3h$ is chosen as the wavelength of the space-domain modulation. In order to force on the frequency range where non-reciprocal wave propagation happens, each PTC disk is grounded with a axial spring ($0.5k_h$) and a torsion spring ($0.5k_m$) to eliminate ultra-low frequency wave branches in the calculated dispersion curves, as shown in Fig. 5b. The dispersion curves for the considered metastructure with time–space modulated prestress is calculated by seeking for a plane wave solution with modulated amplitude [13] and the details can be found in Appendix B. First, non-mirror symmetry for the zero dimensionless wave vector point is noticed in Fig. 5b, which directly indicates that the elastodynamic reciprocity is broken and therefore, left-to-right and right-to-left waves behave differently in the modulated metastructure. Then, particular attention is paid on the gray zone, where the wave branch only appears on the side with positive dimensionless wave vector. This indicates that the wave can only propagate from left to right and asymmetric wave propagation is realized by breaking the time-reciprocal symmetry. Finally, to validate the non-reciprocal wave propagating phenomena, we use fourth order Runge–Kutta method to numerically investigate the transient wave propagation in a metastructure chain consisting of 1800 PTCs and fixed boundaries in both ends. The aforementioned time–space modulated prestress is applied to each PTC of the metastructure. The input is a 100-peak tone burst force excitation with 1170 Hz central frequency, $F_0(1-\cos(2\pi f_c t/100))\times\sin(2\pi f_c t)$. The excitation is applied at the center of the chain. Fig. 5c shows the transient wave results and it can be found that most wave energy is propagating from left to right while almost no energy transmission can be found in the other direction, which agrees well with the dispersion result. Also, it should be mentioned that the size of the metastructure is dependent on several factors, such as the working frequency range, the high/low gradient design which can affect the transmission loss and the modulated frequency in the non-reciprocal system.

4. Conclusions

In this paper, a theoretical model with coupled axial-torsional effective stiffness is first developed to study the prestress-controlled wave selection and conversion phenomena in tensegrity metastructures. Then, asymmetric wave propagation in the metastructure is realized with designed prestress distribution in spatial domain. Finally, the non-reciprocal elastic wave propagation is achieved by expanding the prestress control in both spatial and time domains. Unlike other asymmetric wave structure designs which strongly rely on the expensive microstructures and external control systems, the proposed prestress-controlled tensegrity metastructures have the advantages of easy realization and potentially *in situ* tunability.

Declaration of competing interest

The authors declare that they have no known competing financial interests or personal relationships that could have appeared to influence the work reported in this paper.

Acknowledgments

This work was supported by the National Natural Science Foundation of China (NSFC) (Nos. 11872112, 11632003, U1837602, 11991030, 11991033 and 111 Project B16003). R. Zhu also acknowledges the support from the Start-up fund from Beijing Institute of Technology (Grant No. 2018CX01031).

Appendix A. Transform matrix method for tensegrity metastructure

The Transfer Matrix method is used to model the mechanical behavior of a 1D PTC chains deriving a frequency-dependent function that describes net transmission of an incident harmonic wave from one end of a finite structure through to the receiving end. A lateral view schematic of the PTC chain is presented in Fig. A.1 where an PTC unit cell j is shown to be positioned between an adjacent PTC unit cell $j-1$ at its left and an adjacent PTC unit cell $j+1$ at its right. The jth PTC unit cell has mass m_j, moment of inertia J_j, and effective axial stiffness k_{hj}, effective coupling stiffness k_{cj} and effective rotation stiffness k_{mj}, respectively. The height of every unit cell is h.

The displacement field u_j and rotation field θ_j in the z direction are written as a superposition of forward and backward H-wave and L-wave, which is shown in Eq. (7)

$$\begin{aligned} u_j &= [A_{Lj}^{+}P_{Luj}e^{iq_{Lj}z}+A_{Lj}^{-}P_{Luj}e^{-iq_{Lj}z}+A_{Hj}^{+}P_{Huj}e^{iq_{Hj}z}+A_{Hj}^{-}P_{Huj}e^{-iq_{Hj}z}]e^{-i\omega t} \\ \theta_j &= [A_{Lj}^{+}P_{L\theta j}e^{iq_{Lj}z}+A_{Lj}^{-}P_{L\theta j}e^{-iq_{Lj}z}+A_{Hj}^{+}P_{H\theta j}e^{iq_{Hj}z}+A_{Hj}^{-}P_{H\theta j}e^{-iq_{Hj}z}]e^{-i\omega t} \end{aligned} \tag{A.1}$$

Where

$$P_{Huj}=\left(\frac{\widetilde{u}}{\sqrt{\widetilde{u}^2+\widetilde{\theta}^2}}\right)_{Hj},\ P_{H\theta j}=\left(\frac{\widetilde{\theta}}{\sqrt{\widetilde{u}^2+\widetilde{\theta}^2}}\right)_{Hj},$$
$$P_{Luj}=\left(\frac{\widetilde{u}}{\sqrt{\widetilde{u}^2+\widetilde{\theta}^2}}\right)_{Lj},\ P_{L\theta j}=\left(\frac{\widetilde{\theta}}{\sqrt{\widetilde{u}^2+\widetilde{\theta}^2}}\right)_{Lj}$$

ω is the angular frequency of the wave, q_{Hj} and q_{Lj} are the wave number of the H-wave and L-wave in the jth PTC unit cell, which can be calculated by Eq. (5). $A_{Lj}^{+}, A_{Lj}^{-}, A_{Hj}^{+}, A_{Hj}^{-}$ are the amplitude of forward and backward of H-wave and L-wave in jth unit cell, respectively.

Calculating the force and torque in the boundaries of the jth unit cell, omitted $e^{i\omega t}$ part, the relationship between displacement, rotation angle, force, torque in the left side of the unit cell and amplitude of the wave can be given as follow:

$$\begin{bmatrix} u_{jleft} \\ \theta_{jleft} \\ F_{jleft} \\ T_{jleft} \end{bmatrix} = \left[B_{jleft}\right] \begin{bmatrix} A_{H+}^{j} \\ A_{H-}^{j} \\ A_{L+}^{j} \\ A_{L-}^{j} \end{bmatrix} \tag{A.2}$$

Where the coefficient matrix

$$\left[B_{jleft}\right] = [D_{jleft}][E_j] \tag{A.3}$$

where (see Box I). The stiffness coefficients are given as follow:

$$k_{FHj}=k_{hj}P_{Hju}+k_{cj}P_{Hj\theta},\ k_{FLj}=k_{hj}P_{Lju}+k_{cj}P_{Lj\theta},$$
$$k_{THj}=k_{cj}P_{Hju}+k_{mj}P_{Hj\theta},\ k_{TLj}=k_{cj}P_{Lju}+k_{mj}P_{Lj\theta}$$

By the same method, the relationship between displacement, rotation angle, force, torque in the right side of the unit cell and amplitude of the wave can be given as follow:

$$\begin{bmatrix} u_{jright} \\ \theta_{jright} \\ F_{jright} \\ T_{jright} \end{bmatrix} = \left[B_{jright}\right] \begin{bmatrix} A_{H+}^{j} \\ A_{H-}^{j} \\ A_{L+}^{j} \\ A_{L-}^{j} \end{bmatrix} \tag{A.4}$$

Where the coefficient matrix (see Box II):

Consider the displacement, rotation angle, force and torque continuous in the boundary,

$$\begin{bmatrix} u_{jright} \\ \theta_{jright} \\ F_{jright} \\ T_{jright} \end{bmatrix} = \begin{bmatrix} u_{j+1\mathrm{left}} \\ \theta_{j+1\mathrm{left}} \\ F_{j+1left} \\ T_{j+1left} \end{bmatrix} \tag{A.5}$$

the transfer matrix between the jth and $j+1$th unit cell can be given as follow

$$\begin{bmatrix} A_{H+}^{j} \\ A_{H-}^{j} \\ A_{L+}^{j} \\ A_{L-}^{j} \end{bmatrix} = \left[B_{j+1left}\right]^{-1}\left[B_{jright}\right] \begin{bmatrix} A_{H+}^{j} \\ A_{H-}^{j} \\ A_{L+}^{j} \\ A_{L-}^{j} \end{bmatrix} \tag{A.6}$$

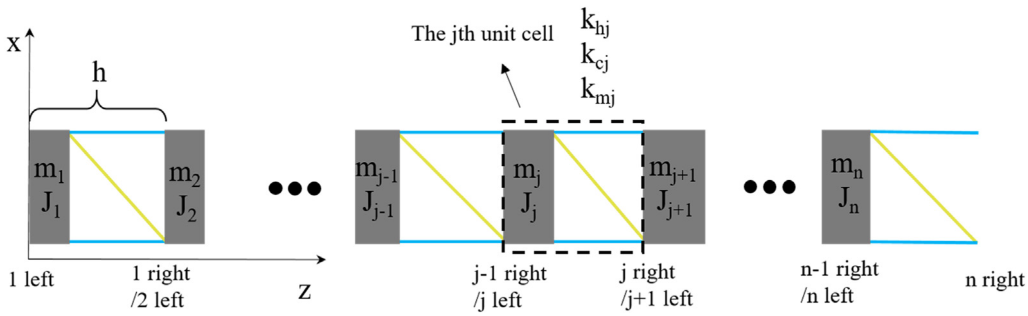

Fig. A.1. Lateral view schematic of the PTC chain.

$$[E_j] = \begin{bmatrix} e^{iq_{Hj}(j-1)h} & 0 & 0 & 0 \\ 0 & e^{-iq_{Hj}(j-1)h} & 0 & 0 \\ 0 & 0 & e^{iq_{Lj}(j-1)h} & 0 \\ 0 & 0 & 0 & e^{-iq_{Lj}(j-1)h} \end{bmatrix}$$

$$\left[D_{jleft}\right] = \begin{bmatrix} P_{Huj} & P_{Huj} & P_{Luj} & P_{Luj} \\ P_{H\theta j} & P_{H\theta j} & P_{L\theta j} & P_{L\theta j} \\ k_{FHj}(e^{iq_{Hj}h}-1)+m_j\omega^2 P_{Huj} & k_{FHj}(e^{-iq_{Hj}h}-1)+m_j\omega^2 P_{Huj} & k_{FLj}(e^{iq_{Lj}h}-1)+m_j\omega^2 P_{Luj} & k_{FLj}(e^{-iq_{Lj}h}-1)+m_j\omega^2 P_{Luj} \\ k_{THj}(e^{iq_{Hj}h}-1)+J_j\omega^2 P_{H\theta j} & k_{THj}(e^{-iq_{Hj}h}-1)+J_j\omega^2 P_{H\theta j} & k_{TLj}(e^{iq_{Lj}h}-1)+J_j\omega^2 P_{L\theta j} & k_{TLj}(e^{-iq_{Lj}h}-1)+J_j\omega^2 P_{L\theta j} \end{bmatrix}$$

Box I.

$$\left[B_{jright}\right] = [D_{jright}][E_j]$$

$$\left[D_{j,\mathrm{right}}\right] = \begin{bmatrix} P_{Hju}e^{iq_{Hj}h} & P_{Hju}e^{-iq_{Hj}h} & P_{Lju}e^{iq_{Lj}h} & P_{Lju}e^{-iq_{Lj}h} \\ P_{Hj\theta}e^{iq_{Hj}h} & P_{Hj\theta}e^{-iq_{Hj}h} & P_{Lj\theta}e^{iq_{Lj}h} & P_{Lj\theta}e^{-iq_{Lj}h} \\ k_{FHj}(e^{iq_{Hj}h}-1) & k_{FHj}(e^{-iq_{Hj}h}-1) & k_{FLj}(e^{iq_{Lj}h}-1) & k_{FLj}(e^{-iq_{Lj}h}-1) \\ k_{THj}(e^{iq_{Hj}h}-1) & k_{THj}(e^{-iq_{Hj}h}-1) & k_{TLj}(e^{iq_{Lj}h}-1) & k_{TLj}(e^{-iq_{Lj}h}-1) \end{bmatrix}$$

Box II.

By iterative use the Eq. (A.6), the transfer matrix between the first and nth unit cell can be given as follow:

$$\begin{bmatrix} A^1_{H+} \\ A^1_{H-} \\ A^1_{L+} \\ A^1_{L-} \end{bmatrix} = [T] \begin{bmatrix} A^n_{H+} \\ A^n_{H-} \\ A^n_{L+} \\ A^n_{L-} \end{bmatrix} \tag{A.7}$$

where

$$[T] = [B_{2left}]^{-1}[B_{1right}][B_{3left}]^{-1}[B_{2right}]\dots[B_{nleft}]^{-1}[B_{n-1right}]$$

$[T]$ is a 4×4 matrix, an assumption that the metastructure has no reflection in both sides. Then the Eq. (A.7) can be simplified as follow

$$\begin{bmatrix} A^1_{H+} \\ A^1_{L+} \end{bmatrix} = \begin{bmatrix} T_{(1,1)} & T_{(1,3)} \\ T_{(3,1)} & T_{(3,3)} \end{bmatrix} \begin{bmatrix} A^n_{H+} \\ A^n_{L+} \end{bmatrix} \tag{A.8}$$

The transmission of H-wave and L-wave for arbitrarily input can be given by Eq. (A.8).

Appendix B. Dispersion curve calculated for time–space modulated prestress tensegrity metastructure

In this part, we main follow Vila's work [13], and calculated the dispersion curve of the metastructure with periodic time modeled prestress, which is showed in Fig. 5a. So that, all three stiffness coefficients that vary in time, and by constant inertia coefficients. The prestress modulation is expressed as a traveling wave propagating with velocity $v_m = WL_m/Tm$, where $WL_m = 3h$ and T_m respectively denote the spatial wavelength and temporal period of the modulation. Thus, at any given instant of time, it is possible to describe the structure as the assembly of unit cells that are identified by one spatial modulation period $3h$. Based on this description, the motion for the nth cell of the assembly can be expressed as

$$\mathbf{M}\ddot{\mathbf{u}}_n + \mathbf{K}^{(l)}_h(t)\mathbf{u}_{n-1} + \mathbf{K}_h(t)\mathbf{u}_n + \mathbf{K}^{(r)}_h(t)\mathbf{u}_{n+1} + \mathbf{K}^{(l)}_c(t)\boldsymbol{\theta}_{n-1} + \mathbf{K}_c(t)\boldsymbol{\theta}_n + \mathbf{K}^{(r)}_c(t)\boldsymbol{\theta}_{n+1} = 0 \tag{B.1}$$

$$\mathbf{J}\ddot{\boldsymbol{\theta}}_n + \mathbf{K}^{(l)}_c(t)\mathbf{u}_{n-1} + \mathbf{K}_c(t)\mathbf{u}_n + \mathbf{K}^{(r)}_c(t)\mathbf{u}_{n+1} + \mathbf{K}^{(l)}_m(t)\boldsymbol{\theta}_{n-1} + \mathbf{K}_m(t)\boldsymbol{\theta}_n + \mathbf{K}^{(r)}_m(t)\boldsymbol{\theta}_{n+1} = 0 \tag{B.2}$$

where $\mathbf{M}$, $\mathbf{K}_h$, $\mathbf{K}_c$, $\mathbf{K}_m$, $\mathbf{u}_n$ and $\boldsymbol{\theta}_n$ denote the mass, compression stiffness matrices, coupling stiffness matrices, rotation stiffness matrices, a vector of displacement of the unit cell n and a vector of rotation angle degrees of freedom of the unit cell n. The stiffness matrices are all expressed as a periodic functions of time with period T_m so that the following relation holds

$$\begin{aligned} \mathbf{K}_h(t) &= \mathbf{K}_h(t + T_m) \\ \mathbf{K}_c(t) &= \mathbf{K}_c(t + T_m) \\ \mathbf{K}_m(t) &= \mathbf{K}_h(t + T_m) \end{aligned} \tag{B.3}$$

$$\begin{bmatrix} \mathbf{K}_h^{(l)}(t)e^{-i3qnh}+\mathbf{K}_h(t)+\mathbf{K}_h^{(r)}(t)e^{i3qnh} & \mathbf{K}_c^{(l)}(t)e^{-i3qnh}+\mathbf{K}_c(t)+\mathbf{K}_c^{(r)}(t)e^{i3qnh} \\ \mathbf{K}_c^{(l)}(t)e^{-i3qnh}+\mathbf{K}_c(t)+\mathbf{K}_c^{(r)}(t)e^{i3qnh} & \mathbf{K}_m^{(l)}(t)e^{-i3qnh}+\mathbf{K}_m(t)+\mathbf{K}_m^{(r)}(t)e^{i3qnh} \end{bmatrix} \begin{Bmatrix} \mathbf{u}_n(t) \\ \boldsymbol{\theta}_n(t) \end{Bmatrix} + \begin{bmatrix} \mathbf{M} & \mathbf{0} \\ \mathbf{0} & \mathbf{J} \end{bmatrix} \begin{Bmatrix} \ddot{\mathbf{u}}_n(t) \\ \ddot{\boldsymbol{\theta}}_n(t) \end{Bmatrix} = \mathbf{0} \tag{B.4}$$

Box III.

Accordingly, each of the matrices in Eqs. (B.1) and (B.2) can be expanded in terms of their Fourier series and expressed as

$$\begin{aligned} &\mathbf{K}_h^{(l)}(t)=\sum_{s=-\infty}^{\infty} e^{is\omega_m t}\mathbf{K}_{hs}^{(l)},\ \mathbf{K}_h(t)=\sum_{s=-\infty}^{\infty} e^{is\omega_m t}\mathbf{K}_{hs}, \\ &\mathbf{K}_h^{(r)}(t)=\sum_{s=-\infty}^{\infty} e^{is\omega_m t}\mathbf{K}_{hs}^{(r)}, \\ &\mathbf{K}_c^{(l)}(t)=\sum_{s=-\infty}^{\infty} e^{is\omega_m t}\mathbf{K}_{cs}^{(l)},\ \mathbf{K}_c(t)=\sum_{s=-\infty}^{\infty} e^{is\omega_m t}\mathbf{K}_{cs}, \\ &\mathbf{K}_c^{(r)}(t)=\sum_{s=-\infty}^{\infty} e^{is\omega_m t}\mathbf{K}_{cs}^{(r)} \\ &\mathbf{K}_m^{(l)}(t)=\sum_{s=-\infty}^{\infty} e^{is\omega_m t}\mathbf{K}_{ms}^{(l)},\ \mathbf{K}_m(t)=\sum_{s=-\infty}^{\infty} e^{is\omega_m t}\mathbf{K}_{ms}, \\ &\mathbf{K}_m^{(r)}(t)=\sum_{s=-\infty}^{\infty} e^{is\omega_m t}\mathbf{K}_{ms}^{(r)} \end{aligned} \tag{B.5}$$

Where $\omega_m = 2\pi/T_m$ is the frequency associated with the temporal modulation. The dispersion relations for the considered time-varying structure can be estimated, following the Hill-determinant method, by seeking for a plane wave solution with modulated amplitude, which is expressed as

$$\mathbf{u}_n(t)=\mathbf{a}(t)e^{i(3nqh+\omega t)},\ \boldsymbol{\theta}_n(t)=\mathbf{b}(t)e^{i(3nqh+\omega t)} \tag{B.6}$$

where $\mathbf{a}(t)=\mathbf{a}(t+T_m)$, $\mathbf{b}(t)=\mathbf{b}(t+T_m)$ is two periodic amplitude functions in time. The frequencies in the displacement amplitude $\mathbf{a}(t)$ and rotation angle amplitude $\mathbf{b}$(t) depend on the stiffness modulation frequency $\omega_m = 2\pi/T_m$ and it can be expressed as a Fourier series in form

$$\mathbf{a}(t)=\sum_{z=-\infty}^{\infty}\mathbf{a}_z e^{iz\omega_m t},\ \mathbf{b}(t)=\sum_{z=-\infty}^{\infty}\mathbf{b}_z e^{iz\omega_m t} \tag{B.7}$$

Based on the Bloch theory

$$\begin{aligned} &\mathbf{u}_{n+1}(t)=e^{i3qh}\mathbf{u}_n(t),\ \mathbf{u}_{n-1}(t)=e^{-i3qh}\mathbf{u}_n(t) \\ &\boldsymbol{\theta}_{n+1}(t)(t)=e^{i3qh}\boldsymbol{\theta}_n(t),\ \boldsymbol{\theta}_{n-1}(t)=e^{-i3qh}\boldsymbol{\theta}_n(t) \end{aligned} \tag{B.8}$$

Substituting into Eqs. (B.1) and (B.2) gives as in Box III which may be written as

$$\begin{bmatrix} \hat{\mathbf{K}}_h(q,t) & \hat{\mathbf{K}}_c(q,t) \\ \hat{\mathbf{K}}_c(q,t) & \hat{\mathbf{K}}_m(q,t) \end{bmatrix} \begin{Bmatrix} \mathbf{u}_n(t) \\ \boldsymbol{\theta}_n(t) \end{Bmatrix} + \begin{bmatrix} \mathbf{M} & \mathbf{0} \\ \mathbf{0} & \mathbf{J} \end{bmatrix} \begin{Bmatrix} \ddot{\mathbf{u}}_n(t) \\ \ddot{\theta}_n(t) \end{Bmatrix} = \mathbf{0} \tag{B.9}$$

where

$$\begin{aligned} &\hat{\mathbf{K}}_h(q,t)=\mathbf{K}_h^{(l)}(t)e^{-i3qnh}+\mathbf{K}_h(t)+\mathbf{K}_h^{(r)}(t)e^{i3qnh} \\ &\hat{\mathbf{K}}_c(q,t)=\mathbf{K}_c^{(l)}(t)e^{-i3qnh}+\mathbf{K}_c(t)+\mathbf{K}_c^{(r)}(t)e^{i3qnh} \\ &\hat{\mathbf{K}}_m(q,t)=\mathbf{K}_m^{(l)}(t)e^{-i3qnh}+\mathbf{K}_m(t)+\mathbf{K}_m^{(r)}(t)e^{i3qnh} \end{aligned}$$

Next, substituting Eq. (B.6) into Eq. (B.9) and performing harmonic balance, by collecting the terms with frequency $\omega + z\omega_m$ we reach

$$-(\omega+z\omega_m)^2 \begin{bmatrix} \mathbf{M} & \mathbf{0} \\ \mathbf{0} & \mathbf{J} \end{bmatrix} \begin{Bmatrix} \mathbf{a}_z \\ \mathbf{b}_z \end{Bmatrix} + \sum_{s=-\infty}^{\infty} \begin{bmatrix} \hat{\mathbf{K}}_{hs}(q) & \hat{\mathbf{K}}_{cs}(q) \\ \hat{\mathbf{K}}_{cs}(q) & \hat{\mathbf{K}}_{ms}(q) \end{bmatrix} \begin{Bmatrix} \mathbf{a}_{z-s} \\ \mathbf{b}_{z-s} \end{Bmatrix} = \mathbf{0} \tag{B.10}$$

Choosing a truncation order Z for the amplitude $\mathbf{a}(t)$ and $\mathbf{b}(t)$, i.e., $\mathbf{a}_p = \mathbf{0}$ and $\mathbf{b}_p = \mathbf{0}$ for $|z| \le Z$. The solution of the following quadratic eigenvalue problem with truncated terms.

$$-(\omega+z\omega_m)^2 \begin{bmatrix} \mathbf{M} & \mathbf{0} \\ \mathbf{0} & \mathbf{J} \end{bmatrix} \begin{Bmatrix} \mathbf{a}_z \\ \mathbf{b}_z \end{Bmatrix} + \sum_{s=-Z+z}^{Z+z} \begin{bmatrix} \hat{\mathbf{K}}_{hs}(q) & \hat{\mathbf{K}}_{cs}(q) \\ \hat{\mathbf{K}}_{cs}(q) & \hat{\mathbf{K}}_{ms}(q) \end{bmatrix} \begin{Bmatrix} \mathbf{a}_{z-s} \\ \mathbf{b}_{z-s} \end{Bmatrix} = \mathbf{0} \tag{B.11}$$

$Z = 1$ is chosen in the study. Then the compression stiffness matrix is given as follow:

$$\begin{aligned} &\hat{\mathbf{K}}_{hs}(q) \\ &= 0.5k_h\mathbf{I}\delta_{s,0} + k_h \begin{bmatrix} 2 & -1 & -e^{-i3qh} \\ -1 & 2 & -1 \\ -e^{i3qh} & 1 & 2 \end{bmatrix} \delta_{s,0} \\ &+ dk_h \begin{bmatrix} e^{is2\pi/3}+e^{is2\pi} & -e^{is2\pi/3} & -e^{-is2\pi}e^{-i3qh} \\ -e^{is2\pi/3} & e^{is4\pi/3}+e^{is2\pi/3} & -e^{is4\pi/3} \\ -e^{-is2\pi}e^{i3qh} & -e^{is4\pi/3} & e^{is2\pi}+e^{is4\pi/3} \end{bmatrix} \delta_{s,\pm 1} \end{aligned} \tag{B.12}$$

The coupling stiffness matrix is given as follow:

$$\begin{aligned} &\hat{\mathbf{K}}_{cs}(q) \\ &= k_c \begin{bmatrix} 2 & -1 & -e^{-i3qh} \\ -1 & 2 & -1 \\ -e^{i3qh} & 1 & 2 \end{bmatrix} \delta_{s,0} \\ &+ dk_c \begin{bmatrix} e^{is2\pi/3}+e^{is2\pi} & -e^{is2\pi/3} & -e^{-is2\pi}e^{-i3qh} \\ -e^{is2\pi/3} & e^{is4\pi/3}+e^{is2\pi/3} & -e^{is4\pi/3} \\ -e^{-is2\pi}e^{i3qh} & -e^{is4\pi/3} & e^{is2\pi}+e^{is4\pi/3} \end{bmatrix} \delta_{s,\pm 1} \end{aligned} \tag{B.13}$$

The rotation stiffness matrix is given as follow:

$$\begin{aligned} &\hat{\mathbf{K}}_{ms}(q) \\ &= 0.5k_m\mathbf{I}\delta_{s,0} + k_m \begin{bmatrix} 2 & -1 & -e^{-i3qh} \\ -1 & 2 & -1 \\ -e^{i3qh} & 1 & 2 \end{bmatrix} \delta_{s,0} \\ &+ dk_m \begin{bmatrix} e^{is2\pi/3}+e^{is2\pi} & -e^{is2\pi/3} & -e^{-is2\pi}e^{-i3qh} \\ -e^{is2\pi/3} & e^{is4\pi/3}+e^{is2\pi/3} & -e^{is4\pi/3} \\ -e^{-is2\pi}e^{i3qh} & -e^{is4\pi/3} & e^{is2\pi}+e^{is4\pi/3} \end{bmatrix} \\ &\times \delta_{s,\pm 1} \end{aligned} \tag{B.14}$$

Thus leads to $6 \times (2Z+1)$ eigenvalues that are of the general form

$$\lambda_{r,z} = \omega_r + z\omega_m \tag{B.15}$$

With $r = 1, 2, 3,\ text and\ z = -1, 0, 1$. The associated eigenvectors $\mathbf{a}_{r,z}$ *and* $\mathbf{b}_{r,z}$, can be expressed as:

$$\begin{aligned} a_{r,z} &= [a^z_{-Z}, \dots, a^z_0, \dots, a^z_{+Z}]^T_r \\ b_{r,z} &= [b^z_{-Z}, \dots, b^z_0, \dots, b^z_{+Z}]^T_r \end{aligned} \tag{B.16}$$

Then, by solving eigenvalue problem obtained from the Eq. (B.11), the dispersion result of the metastructure with periodic time modulated prestress can be obtain, which is shown in Fig. 5b.

References

[1] J.D. Achenbach, Reciprocity in Elastodynamics, Cambridge University Press, 2003.
[2] J.D. Achenbach, Wave Propagation in Elastic Solids, Elsevier Science, 1973.
[3] A.T. de Hoop, Handbook of Radiation and Scattering of Waves, Academic Press, 1995.
[4] G. Trainiti, M. Ruzzene, Non-reciprocal elastic wave propagation in spatiotemporal periodic structures, New J. Phys. 18 (2016) 83047.
[5] K. Yi, S. Karkar, M. Collet, One-way energy insulation using time-space modulated structures, J. Sound Vib. 429 (2018) 162–175.
[6] J. Huang, X.M. Zhou, A time-varying mass metamaterial for non-reciprocal wave propagation, Int. J. Solids Struct. 164 (2019) 25–36.
[7] P.A. Deymier, V. Gole, P. Lucas, J.O. Vasseur, K. Runge, Tailoring phonon band structures with broken symmetry by shaping spatiotemporal modulations of stiffness in a one-dimensional elastic waveguide, Phys. Rev. B 96 (2017).
[8] M.A. Attarzadeh, M. Nouh, Non-reciprocal elastic wave propagation in 2D phononic membranes with spatiotemporally varying material properties, J. Sound Vib. 422 (2018) 264–277.
[9] A.A. Maznev, A.G. Every, O.B. Wright, Reciprocity in reflection and transmission: what is a phonon diode? Wave Motion 50 (2013) 776–784.
[10] X. Zhu, X. Zou, B. Liang, J. Cheng, One-way mode transmission in one-dimensional phononic crystal plates, J. Appl. Phys. 108 (2010) 124909.
[11] N. Boechler, G. Theocharis, C. Daraio, Bifurcation-based acoustic switching and rectification, Nature Mater. 10 (2011) 665–668.
[12] S.P. Wallen, M.R. Haberman, Nonreciprocal wave phenomena in spring-mass chains with effective stiffness modulation induced by geometric nonlinearity, Phys. Rev. E. 99 (2019) 013001.
[13] J. Vila, R.K. Pal, M. Ruzzene, G. Trainiti, A Bloch-based procedure for dispersion analysis of lattices with periodic time-varying properties, J. Sound Vib. 406 (2017) 363–377.
[14] H. Nassar, H. Chen, A.N. Norris, M.R. Haberman, G.L. Huang, Non-reciprocal wave propagation in modulated elastic metamaterials, Proc. R. Soc. Lond. Ser. A Math. Phys. Eng. Sci. 473 (2017) 0188.
[15] H. Nassar, H. Chen, A.N. Norris, G.L. Huang, Non-reciprocal flexural wave propagation in a modulated metabeam, Extreme Mech. Lett. 15 (2017) 97–102.
[16] H. Nassar, X.C. Xu, A.N. Norris, G.L. Huang, Modulated phononic crystals: Non-reciprocal wave propagation and Willis materials, J. Mech. Phys. Solids 101 (2017) 10–29.
[17] K. Yi, M. Ouisse, E. Sadoulet-Reboul, G. Matten, Active metamaterials with broadband controllable stiffness for tunable band gaps and non-reciprocal wave propagation, Smart Mater. Struct. 28 (2019) 065025.
[18] Y.F. Wang, B. Yousefzadeh, H. Chen, H. Nassar, G.L. Huang, C. Daraio, Observation of nonreciprocal wave propagation in a dynamic phononic lattice, Phys. Rev. Lett. 121 (2018) 194301.
[19] G. Trainiti, Y. Xia, J. Marconi, G. Cazzulani, A. Erturk, M. Ruzzene, Time-periodic stiffness modulation in elastic metamaterials for selective wave filtering: theory and experiment, Phys. Rev. Lett. 122 (2019) 124301.
[20] Z. Wang, Q. Zhang, K. Zhang, G. Hu, Tunable digital metamaterial for broadband vibration isolation at low frequency, Adv. Mater. 28 (2016) 9857–9861.
[21] Q. Zhang, Y. Chen, K. Zhang, G. Hu, Programmable elastic valley Hall insulator with tunable interface propagation routes, Extreme Mech. Lett. 28 (2019) 76–80.
[22] A. Bergamini, T. Delpero, L. De Simoni, L. Di Lillo, M. Ruzzene, P. Ermanni, Phononic crystal with adaptive connectivity, Adv. Mater. 2 (2013) 1343–1347.
[23] R. Zhu, Y.Y. Chen, M.V. Barnhart, G.K. Hu, C.T. Sun, G.L. Huang, Experimental study of an adaptive elastic metamaterial controlled by electric circuits, Appl. Phys. Lett. 108 (2016) 011905.
[24] L. Airoldi, M. Ruzzene, Design of tunable acoustic metamaterials through periodic arrays of resonant shunted piezos, New J. Phys. 13 (2011) 113010.
[25] Y.Y. Chen, R. Zhu, M.V. Barnhart, G.L. Huang, Enhanced flexural wave sensing by adaptive gradient-index metamaterials, Sci. Rep. 6 (2016).
[26] W.J. Parnell, A.N. Norris, T. Shearer, Employing pre-stress to generate finite cloaks for antiplane elastic waves, Appl. Phys. Lett. 100 (2012) 171907.
[27] W.J. Parnell, Nonlinear pre-stress for cloaking from antiplane elastic waves, Proc. R. Soc. Lond. Ser. A Math. Phys. Eng. Sci. 468 (2012) 563–580.
[28] K. Bertoldi, M.C. Boyce, Wave propagation and instabilities in monolithic and periodically structured elastomeric materials undergoing large deformations, Phys. Rev. B 78 (2008).
[29] R.K. Pal, M. Ruzzene, J.J. Rimoli, Tunable wave propagation by varying prestrain in tensegrity-based periodic media, Extreme Mech. Lett. 22 (2018) 149–156.
[30] Y.T. Wang, X.N. Liu, R. Zhu, G.K. Hu, Wave propagation in tunable lightweight tensegrity metastructure, Sci. Rep. 8 (2018).
[31] N. Ali, I. Smith, Dynamic behavior and vibration control of a tensegrity structure, Int. J. Solids Struct. 47 (2010) 1285–1296.
[32] L. Zhang, Y. Li, Y. Cao, X. Feng, Stiffness matrix based form-finding method of tensegrity structures, Eng. Struct. 58 (2014) 36–48.
[33] I.J. Oppenheim, W.O. Williams, Geometric effects in an elastic tensegrity structure, J. Elasticity 59 (2000) 51–65.